

EELS: Towards Autonomous Mobility in Extreme Terrain with a Versatile Snake Robot with Resilience to Exteroception Failures

Rohan Thakker*, Michael Paton*, Marlin P. Strub*, Michael Swan*, Guglielmo Daddi*[§], Rob Royce*, Phillipe Tosi, Matthew Gildner, Tiago Vaquero, Marcel Veismann, Peter Gavrilo, Eloise Marteau, Joseph Bowkett, Daniel Loret, Yashwanth Nakka, Benjamin Hockman, Andrew Orekhov[†], Tristan Hasseler, Carl Leake, Benjamin Nuernberger, Pedro Proença, William Reid, William Talbot, Nikola Georgiev, Torkom Pailevanian, Avak Archanian, Eric Ambrose, Jay Jasper, Rachel Etheredge, Christiahn Roman, Dan Levine, Kyohei Otsu, Hovhannes Melikyan, Jeremy Nash, Richard Rieber, Kalind Carpenter, Abhinandan Jain, Lori Shiraishi, Daniel Pastor, Sarah Yearicks, Michel Ingham, Matthew Robinson, Ali Agha, Matthew Travers, Howie Choset[‡], Joel Burdick[‡], Masahiro Ono

Abstract—The discovery of ocean worlds such as Enceladus, Titan, and Europa motivates the development of versatile autonomous mobility systems to enable the next era of space exploration where there is large uncertainty in terrain specifications due to a lack of prior surface reconnaissance missions. To explore these environments, we propose Exobiology Extant Life Surveyor (EELS): the *first* large-scale (4 m long with 400 Nm peak torque) snake robot. The large scale is achieved by using a screw-based active skin mechanism to decouple motion and shape control. Autonomous mobility for such a system remains an open problem due to its many Degrees of Freedom (DoFs), complex terrain interactions, and intermittent localization failures in GPS-denied perceptually degraded environments due to the presence of fog, dust, featureless terrains, etc. We propose *NEO*, an autonomy architecture that scales to large DoFs to generate a versatile set of gaits to achieve mobility in unknown extreme environments. We also discuss the resilience capabilities of NEO that achieves closed-loop tracking performance by leveraging exteroception when available but can also operate with proprioception only, leading to resiliency against localization failures via graceful degradation in performance rather than unsafe behaviors. A quantitative hardware evaluation of exteroceptive leader-follower gait is performed indoors on synthetic ice along with qualitative results of field deployment of the proprioceptive leader-follower and sidewinding gaits in extreme environments of icy and sandy terrains with mobility-stressing elements such as trenches, undulations, and steep slopes (up to 35 degrees). We present a set of lessons learned from field deployments with a summary of challenges and open research problems. Video: www.rohanthakker.in/eels-neo-autonomy.html

I. INTRODUCTION

Exploring ocean worlds in our solar system, such as Enceladus, Europa, or Titan, is arguably our best option to answer a pivotal question that reaches civilization-level science: Are we alone? Due to the lack of prior surface reconnaissance missions, there is significant uncertainty in

*These authors contributed equally to this work.

[‡] Department of Mechanical & Civil Engineering, California Institute of Technology, Pasadena, CA, USA

[†] Robotics Institute, Carnegie Mellon University, Pittsburgh, PA, USA

[§] Department of Mechanical and Aerospace Engineering, Politecnico di Torino, Torino, TO, 10129, Italy

Others: NASA Jet Propulsion Laboratory, California Institute of Technology, Pasadena, CA, USA. rohan.a.thakker@jpl.nasa.gov



Fig. 1: The Exobiology Extant Life Surveyor (EELS) robot traversing over mobility-stressing extreme terrains

the terrain properties of such worlds. Furthermore, the large distance from Earth induces a communication lag that limits significant human-in-the-loop operations and failure responses as frequently performed in Mars/Moon missions. Additionally, plumes discovered at the south pole of Enceladus provide a natural entry into the sub-ice ocean if the mobility system can traverse through holes that are more than 10 cm wide while resisting the potential upward force of the plumes themselves [1].

EELS is a suitable platform for such a mission due to 1) its versatility, enabling a variety of gaits to adapt to a wide variety of terrains; 2) its ability to traverse constrained passages; 3) its large scale of 4m length and 400 N.m. peak torque capability; and 4) its modular hardware architecture with repeated joints that can provide resiliency through redundancy [1], [2], [3].

There is a large body of literature on the design, modeling, and control of snake robots, as reviewed in [4], [5]. Most previous work uses “shape-based locomotion”, relying on the cyclical movement of the robot’s joint angles to generate displacement of the robot’s position. These gaits leverage reactive control policies and generally struggle to navigate steep slopes or avoid hazards such as negative obstacles [6]. Furthermore, these gaits operate the actuators much faster than the quasi-static speeds limiting the torque capacity of their actuators, which prevents building these robots at a large scale.

Screw-driven snake robots not only open the door to large-scale but also to the design of deliberative behaviors. However, these robots have received limited attention in the research community. Prior work includes a recent design called the ARCSnake, which demonstrated the viability of surface locomotion with screws using an architecture similar to the EELS [2]. Control laws for limited surface mobility on flat ground have been developed in [3] and studied for controlling a single module with multiple screws in [7], [8]. Screw actuation has also been studied in surgical applications as a propulsion mechanism for endoscopes [9], [10].

Despite this body of knowledge, the autonomous navigation of a screw-propelled snake robot for a space exploration mission remains unstudied. The problem includes the following challenges: 1) many (≈ 36) Degrees of Freedom (DoFs) in the mechanism, 2) the need to traverse mobility-stressing geometries such as steep slopes, trenches, and undulating terrains with a wide variety of terramechanical properties (Fig. 1) the existence of failures in exteroceptive localization and mapping algorithms in the presence of perceptually challenging conditions of fog, rain, dust, and degenerate geometries (e.g. tubes) [11], [12].

Contributions: In this work, we present the first large-scale (4 m long with 400 Nm peak torque and 100 kg mass) snake robot mobility architecture that achieves scalability to large DoFs by exploiting the physics of a screw mechanism that decouples the motion- and shape-control problem into separate loops. We introduce the NEO Autonomy Architecture designed for versatile robots to operate in unknown extreme environments. Specifically, we present how NEO achieves resilience to failures of exteroception by using a control layer that can operate only on proprioceptive feedback, but leverages exteroceptive planning when available. This allows for graceful degradation of the system in the event of exteroceptive failures, which yields a slight reduction in performance rather than unsafe behaviors or relying on operator intervention. A novel path tracking and motion controller is presented to achieve lower than 0.05m tracking errors when exteroceptive feedback is available.



Fig. 2: The EELS exteroceptive sensor suite containing a 3D LiDar, 4x stereo pairs, and an IMU).

A quantitative experimental evaluation of exteroceptive closed-loop tracking is performed on synthetic ice, along with a qualitative field demonstration of the proprioceptive control layer on ice and sandy terrains. Finally, a summary of the lessons learned and open research problems is presented.

Future Work: Autonomous switching between proprioceptive and exteroceptive modes of operation based on localization failure state and autonomous gait selection is not in-scope of this work and we welcome further research in these areas.

II. EELS HARDWARE

EELS is a novel snake-like robot that was developed at NASA Jet Propulsion Laboratory (JPL). The robot is composed of ten identical modules, an exteroceptive head. Each of the modules has three actuators: two control the shape of the robot and one controls the screws. The robot is unique in its scale: 4m long with 400 N.m. of peak torque, which is enabled using the active-skin design which decouples the shape and motion control. EELS is powered externally via a 50 feet long tether which is an analogue to an Enceladus mission scenario where the external power can be obtained using nuclear energy on a lander.

The shape actuators continuously modify the shape of the robot in a quasi-static fashion while the robot’s propulsion is handled by the screw actuators. Operating the shape actuators in the quasi-static regime allows the actuators to sustain significantly higher loads (2x-3x) compared to their continuous rating. In fact, this would be true for any actuator that features a high latent power ratio gearbox (true for the majority of compact high reduction ratio gearboxes [13]). Hence, EELS’s shape actuators can efficiently support very high loads due to the interaction of the robot with the environment, while the robot is efficiently locomoting using its active skin propulsion system based on high-efficiency planetary gearboxes. This allowed us to scale the robot to a 4m length and 100kg mass.

EELS features an exteroceptive head, shown in Fig. 2, at the leading end of the robot, used to help access and navigate the terrain and obstacles during the mission. This head contains four stereo visual camera pairs and one 3D LIDAR

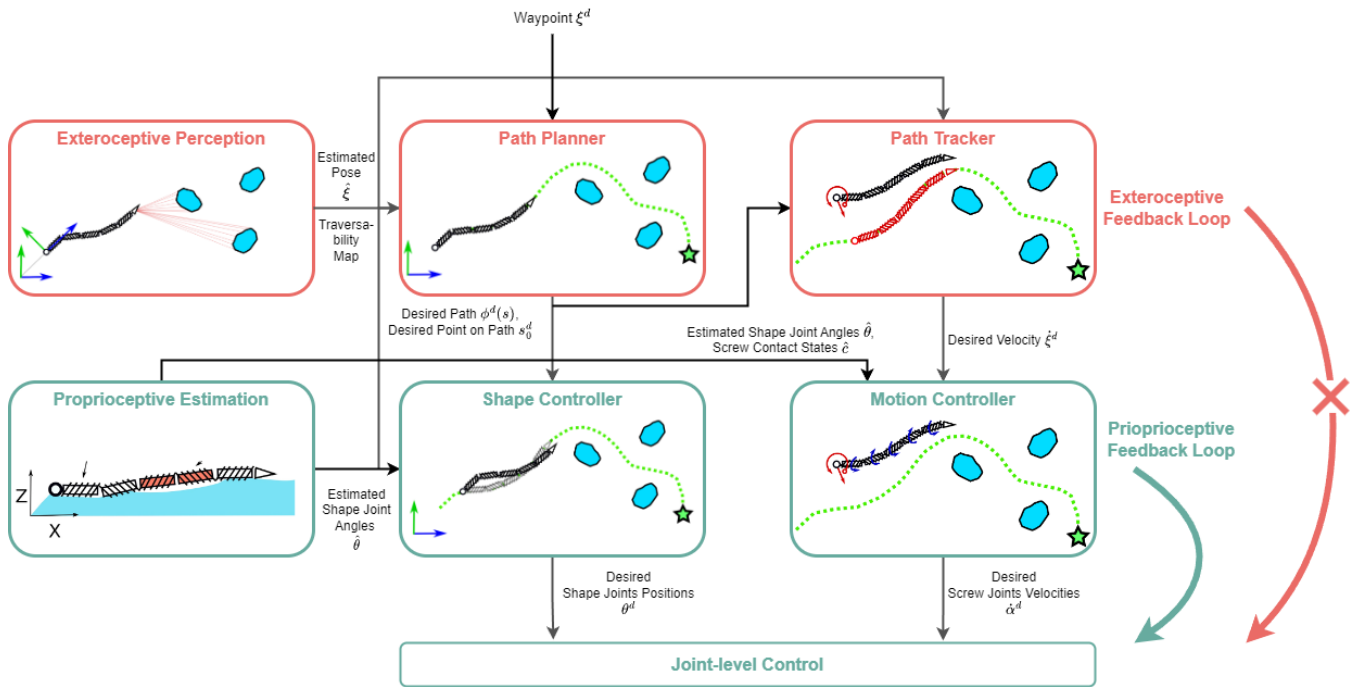


Fig. 3: NEO Autonomy Architecture to achieve versatile locomotion in unknown extreme terrains with resilience to exteroceptive localization failures. Specifically, an implementation is shown to achieve a leader-follower gait that enables the robot’s leader (black triangle) and follower modules to plan and travel along an SE(3) path to a waypoint, ξ^d . The **proprioceptive estimator** uses various sensors to estimate the shape of the robot and the contact states of the screws. The **exteroceptive perception** module estimates pose and computes a traversability map. The collision-free and curvature-constrained paths are computed by the **path planner**. A **path tracker** computes a velocity correction based on the position errors of all modules on the path. A **shape controller** computes the desired shape positions of the robot given its position along the path and sends the desired position commands to the **joint-level controller**. A **motion controller** computes the desired screw-joint velocities given the robot’s current shape and its desired commanded body velocity to progress along the path and make holonomic corrections to stay on the path.

sensor. While in a normal orientation, these sensors are laid out in such a way that one stereo pair and the LIDAR sensor are facing forward, while the remaining three stereo pairs are viewing left, right, and upwards, respectively. Additionally, the head of EELS incorporates an Inertial Measurement Unit (IMU). An onboard computer is used to organize all the data from these sensors and forward it to the motion planner.

III. NEO: EELS AUTONOMY ARCHITECTURE

A. Overview and Resilience to Exteroception Failures

Robust exteroceptive localization and mapping in unstructured icy terrains is still an active area of research. The presence of featureless terrains, fog, and plumes on Enceladus can cause exteroceptive perception systems to fail, resulting in jumps, drift, and, in some cases, complete loss of localization output [12]. Closing high-frequency control loops during such failure events can significantly affect the stability and safety of the robot. However, completely ignoring the exteroceptive estimates can result in significant sub-optimality. The NEO architecture, shown in Fig. 3, exploits the best of both worlds by closing the low-level high-frequency control loops only on proprioceptive estimates and by using the exteroceptive measurements for the higher-level

perception and planning loop that generates the desired state for the proprioceptive layer. This hierarchical approach has two advantages: 1) it allows the robot to continue operation in “blind mode” in the event of exteroception failures to escape the perceptually degraded region, raising the opportunity to recover exteroception, and 2) it provides an ability to leverage the exteroception information when available.

B. Proprioceptive Estimation and Control

1) *Shape Control*: We first describe a *leader-follower* gait that uses the screws to propel EELS along a given reference path. Each module of the EELS robot has one bend and one twist actuator, which control its shape task space 2. Controlling the shape at the joint level is difficult because of the DoFs of the mechanism. Our leader-follower formulation instead controls the shape of the EELS robot in the task space 3.

The approach assumes that both ends of a module are perfectly on the given reference path and that this module is fixed. The controller first calculates the required bend- and twist-joint positions that place the end of the module adjacent to the fixed module onto the reference path by solving the corresponding inverse kinematics problem explained in

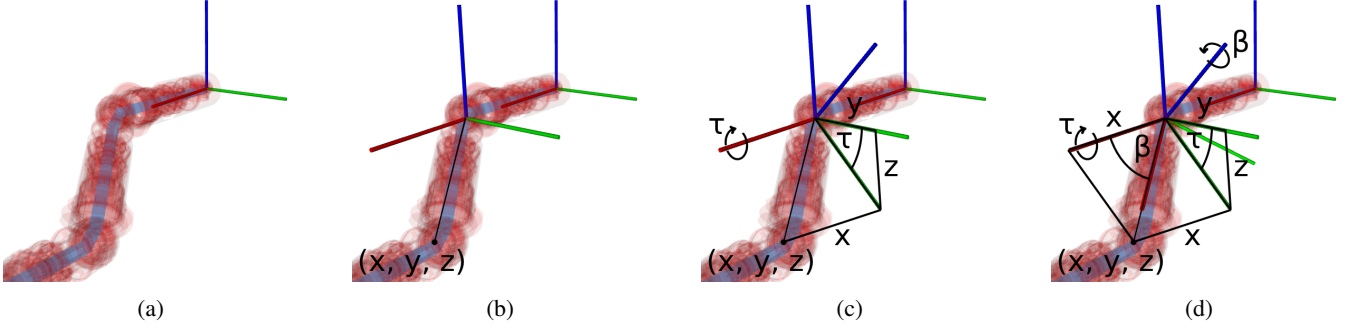


Fig. 4: The task-space shape control approach (Section III-B.1) assumes that one module is fixed on the reference path (a) (blue line). The coordinate frame of that module is translated to the beginning of the next module and the (x, y, z) coordinates of the end of that module are expressed in the coordinates of that frame (b). The desired twist angle, τ , is computed as $\tau = \arctan z/y$ and the coordinate frame is rotated by τ around its x axis (c). The desired bend angle, β , is then computed as $\beta = \arctan \sqrt{y^2+z^2}/x$, and the frame is rotated by β around the twist-adjusted z axis (d). This frame is then assumed to be fixed and the procedure is repeated until the desired twist and bend angles are calculated for all modules.

Fig. 4.

Shape-based sidewinding gait: EELS is not limited to the screw-based leader-follower gait. We have also integrated gaits from prior snake-robot work that locomote primarily using the shape actuators. This is done by offsetting adjacent twist actuators by $\frac{\pi}{2}$ radians such that the axes of adjacent bend actuators are orthogonal. The result is a nominal kinematic configuration similar to prior snake robot designs [14], allowing us to execute gaits previously developed based on the “serpenoid” equation. The serpenoid equation is given as a function of module number n and time t , with seven user-specified parameters:

$$\theta_{bend}(n, t) = \begin{cases} \beta_e + A_e \sin(\omega_s n + \omega_t t) & n = \text{even} \\ \beta_o + A_o \sin(\omega_s n + \omega_t t + \delta) & n = \text{odd} \end{cases} \quad (1)$$

where β_e and β_o are constant offsets, A_e and A_o are amplitudes, w_s is the spatial frequency, w_t is the temporal frequency, and δ is the phase shift. As shown in [15], modifying these parameters can generate a variety of locomoting gaits. Testing on EELS thus far has primarily focused on a “sidewinding” gait, with $\beta_e = \beta_o = 0$, and $\delta = \frac{\pi}{4}$.

2) *Motion Control*: Active-skin allows us to decouple the shape and motion control problem for screw-based gaits. The objective of the motion controller is to track a desired velocity of the floating base $\dot{\xi}$ (our implementation places this at the tail of the robot) by modulating the speed of the screw actuators. We show that this can be achieved by solving a linear system of equations. We formulate the problem by enforcing a no-slip constraint along the direction perpendicular to the blade of the screws in contact with the ground. Fig. 5 shows the coordinate frames of the contact point of the screws. Let $m_i s_j$ be the frame associated with i^{th} module’s j^{th} screw. The no slip constraint for this screw can be written as follows:

$$(v_{m_i s_j})^y = 0 \quad (2)$$

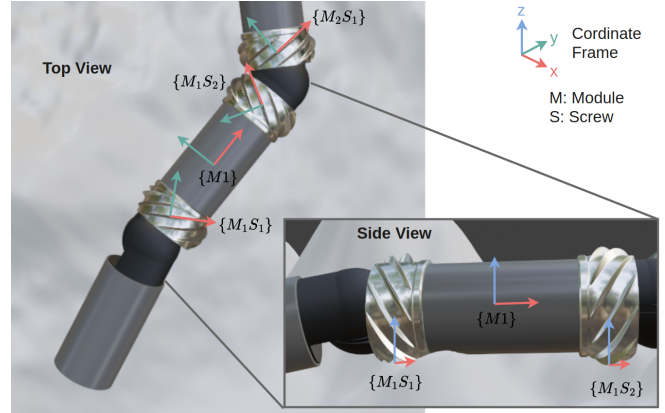


Fig. 5: Screw Frame $\{m_i s_j\}$ is placed at the point of contact with the terrain along the center of the length of the screw.

where $v_{m_i s_j} \in \mathfrak{se}(3) = \mathbb{R}^6$ is the velocity of contact frame $m_i s_j$ of the screws w.r.t. an inertial frame represented in the contact frame. This velocity can be calculated as follows:

$$v_{m_i s_j} = \underbrace{T_{m_0}^{m_i s_j} \dot{\xi}}_{\text{from motion of floating base}} + \underbrace{T_{m_0}^{m_i s_j} J^{m_i s_j} \dot{\theta}_{shape}}_{\text{from motion of shape joints}} + \underbrace{\omega_{m_i s_j} \times R_{m_i s_j}}_{\text{from motion of screw}} \quad (3)$$

Where $T_B^A : \mathbb{R}^6 \rightarrow \mathbb{R}^6$ is the adjoint operator used to transform the velocities from frame B to A . $J^{m_i s_j} : \mathbb{R}^{N_{shape}} \rightarrow \mathbb{R}^6$ is the jacobian of contact frame and $\dot{\theta}_{shape}$ is a vector of velocities of the shape actuators. Finally, $\omega_{m_i s_j} \in \mathbb{R}^6$ is the velocity from the rotation of the screws actuator represented in the contact frame and $R_{m_i s_j}$ is the vector of the radius of the screw represented in the contact frame.

Stacking all the no slip conditions together gives [3]:

$$A(\theta, c)\dot{\xi} = B(\theta, c)\omega_{screw} \quad (4)$$

Where $\omega_{screw} \in \mathbb{R}^{N_{screws}}$ is a vector of all screw joint velocities. Finally, the desired screws velocities are obtained

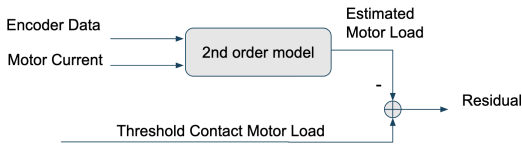


Fig. 6: Contact estimation block diagram

using:

$$\omega_{screw}^d = B^{-1}(\theta, c)A(\theta, c)\dot{\xi}^d \quad (5)$$

The shape controller performs shape adjustments θ and gets sufficient number of screws are in contact c to ensure B^{-1} exists. Note that unlike [3], our formulation doesn't make the planar assumption about the velocities i.e. $\dot{\xi}^d \in \mathfrak{se}(3)$.

3) *Proprioceptive Contact Estimation*: Note that while the motion control algorithm in eq. 5 computes velocities of all the screws, only those screws that are in contact with the surface can propel EELS. A screw is said to be in contact if there is enough traction between the screw and the surface to provide the reaction force for mobility. The contact estimation algorithm estimates whether a screw is in sufficient contact with the surface, as defined earlier. As shown in Fig. 6, we fit a second-order to predict the nominal current of the screw actuator under no contact conditions using the motor currents and encoder data. The screw is considered in contact if the measured screw motor current is significantly higher than that predicted by the model.

4) *Joint Control*: Each of the twist, bend, and screw actuators within a module are controlled via an Elmo MC motor controller [16], which implements the CiA 402 motion control standard [17]. A control computer, in the form of an Intel NUC, interfaces with each of the motor controllers via an EtherCAT bus; with the software stack for the 'master' node within the computer supplied by the JPL-developed FastCAT library [18]. This EtherCAT interface affords low-latency, synchronous communication with each node within the network; at the time of writing this is set to 100Hz, but has allowed operation in similar JPL systems of up to 2kHz control rate.

C. Exteroceptive Planning and Perception

1) *Path Planner*: A major benefit of EELS compared to traditional mobility platforms is its many modes of locomotion which allow it to traverse various types of challenging terrain. This increased versatility results from the many degrees of freedom which in turn result in increased complexity. The combination of many degrees of freedom with the difficult-to-model interactions of the screws with the environment makes designing a path-planning algorithm that can fully leverage the versatility of EELS a challenging problem that is not in the scope of this paper. Instead, this section presents the algorithm that was used to plan paths on the surface for the leader-follower gait shown in Fig. 3.

Focusing on the leader-follower gait for surface operations greatly simplifies the path-planning problem for EELS. Instead of considering all degrees of freedom, the presented

planner only considers the path of the head (i.e., the leader) and assumes that this path is followed by all other modules (i.e., the followers). For the other modules to be able to follow the head, the head must not move backward and following the path must not require shape-joint angles that exceed the joint limits of EELS.

These requirements are satisfied by using a sampling-based planning algorithm, that samples states in $SE(2)$ and connects them with Dubins' curves [19]. The planner uses the traversability layer described in Section III-C to lift the path to $SE(3)$ using the terrain geometry and discard states and connections that are considered unsafe. The optimization objective used in the planner combines path length with a cost from the traversability layer. It assigns each path, $\sigma: [0, 1] \rightarrow SE(3)$, a cost that is computed as

$$\int_0^l 1 + w_t t(\sigma_p(s/l)) ds, \quad (6)$$

where l is the length of the path, $w_t \geq 0$ is a user-specified weight for the traversability term, $t: \mathbb{R}^3 \rightarrow [0, 1]$ is a traversability cost, and $\sigma_p: [0, 1] \rightarrow \mathbb{R}^3$ is the position component of the $SE(3)$ path.

This optimization objective allows using the length of Dubins' path between two states as an admissible cost heuristic in the planning algorithm. This additional information was leveraged by using Advanced Batch Informed Trees (ABIT*) [20] as the planning algorithm with the implementation provided by the Open Motion Planning Library (OMPL v1.5) [21], with all default parameters except that ABIT* was configured to sample deterministic states based on the Halton sequence [22]. Rejection sampling was used to ensure that sampled states are in the informed set [23].

2) *Path Tracker*: The screw-control algorithm (Section III-B.2) enables holonomic motion for the floating base of the robot. The path-tracking controller takes advantage of this property to make rigid-body corrections to stay on the path while operating in leader-follower mode. The path-tracking algorithm is illustrated in Fig. 3. The controller first computes the desired position of the robot (red robot), as the position on the reference path that is closest to the current position of the robot (black robot). Next, both current and desired robot module poses are represented as point clouds (black and red circles). A rigid $SE(3)$ transformation between current and desired is computed using the closed-form solution to align point clouds with known correspondences formulated in [24]. We use a proportional control law to convert this $SE(3)$ pose to a $\mathfrak{se}(3)$ velocity that is sent to the screw-control algorithm to correct for path-tracking errors.

3) *Multi-sensor SLAM*: The EELS robot is designed to navigate perceptually degraded glacial terrain such as flat expanses of ice and conduits with repeating tunnel-like geometries. To navigate these challenging terrains, the EELS autonomy system makes use of a multi-sensor Simultaneous Localisation And Mapping (SLAM) solution called State Estimation through Robust Perception in Extreme and Novel Terrains (SERPENT)[25]. The SERPENT algorithm gains resiliency against perceptually-degraded environments through

an uncertainty-aware tightly-coupled fusion of LiDAR, IMU, Stereo, and altimeter data.

4) *Traversability Analysis*: The path planner reasons about obstacles using the Elevation Mapping and Traversability Analysis approach described in [26] i.e. implemented using [27]. Filtered LiDAR pointclouds and state estimates from SERPENT are sent to the Elevation mapping module to compute 2.5D elevation maps centered around the robot. Slope- and step-hazard layers are then computed and added to the map before sending to the planner.

IV. EXPERIMENTS AND RESULTS

We evaluate the performance of NEO by performing two categories of experiments: i) a qualitative analysis of proprioceptive estimation and controls layer from section III-B on challenging field environments (ice, snow, and sand). Specifically, we tested the leader-follower screw-based gait and sidewinding shape-based gait with the exteroceptive sensor head completely removed. ii) a quantitative analysis of the exteroceptive and proprioceptive layers (Fig. 3) on the synthetic ice terrain.

A. Field Demonstrations of Proprioception Layer

Field Locations All experiments were conducted in three unique field locations: 1) Big Bear: (Fig. 7.a,f) consisted of a mixture of consolidated and unconsolidated snowy terrain with trenches longer than the robot and roughly the height of the robot module. 2) Table Mountain: consisted of a steep slope (up to 35 deg) of unconsolidated snow (Fig. 7.b), a globally planar ice rink with local undulations and bumps (Fig. 7.c), and a shallow slope with repeating undulations up to 0.75 m high. 3) Mars yard: testing area consisted of both consolidated and unconsolidated sand (Fig. 7.d, 7.e).

Qualitative Analysis: We evaluate the performance of the sidewinding and leader-follower gait’s ability to make forward progress in these challenging terrains through a qualitative analysis of the videos that generated the timelapse imagery in Fig. 7. We look at two primary metrics, listed in Table I, to evaluate forward locomotion: distance traversed, and average speed. In Experiments 1-4, we evaluate the performance of the leader-follower gait’s ability to make forward progress in various undulating terrain types. In Experiments 5 and 6, we evaluate the performance of the sidewinding gait’s ability to overcome terrain: a robot-sized trench at table mountain in Experiment 5, and sand in the Mars Yard in Experiment 6. This relatively slow speed is due to the robot becoming briefly stuck in the trench until it was able to lift itself out. These experiments highlight the EELS robot’s ability to recover from stuck situations in difficult real-world terrains using shape actuators.

B. Quantitative Evaluation of Exteroceptive + Proprioceptive Layers on Synthetic Ice

Testing Environment: The experiments were conducted in a laboratory environment with planar simulated synthetic ice panels, which are used by ice skaters. In tests 1-5, the leader-follower gait was used to follow a fixed, obstacle-free

path from a fixed start and goal location. In tests 6-9, the leader-follower gait was used to navigate to a waypoint on the other side of an obstacle field, with the ability to replan its path if new obstacles emerge in the map. In test 10, the leader-follower gait with *no* exteroceptive feedback was used to navigate to a waypoint on the other side of the obstacle field. An overview of these tests can be seen in Fig. 8.

Quantitative Analysis: Results of the leader-follower gaits for both experiments can be found in Table II. For all experiments we show the following metrics: i) the distance the rover drove to arrive at the goal, ii) the number of autonomous path replans that occurred, iii) the number of manual interventions required, and iv) the mean, std. dev., and max path-tracking error of *each* module’s position to the path. In experiments 1-5 where there were no obstacles in the scene, the rover’s mean path tracking error stayed below 6.7 cm and no manual interventions were required to arrive at the goal. In experiments 6-10 while avoiding obstacles, the rover’s mean path tracking error stayed below 2.9 cm, with manual interventions ranging from zero to three per run. In experiments, 6 and 8, the rover successfully drove from the start to the goal while avoiding obstacles with no manual interventions required to avoid obstacles. Experiment 7 required three manual interventions to arrive at the goal. The first was due to a controller bug that caused the front half of the robot to straighten out. This has since been fixed. The latter two interventions were due to close proximity to obstacles. This was due to a lack of robot inflation in the obstacle map, causing the planner to “hug” corners around obstacles to optimize the path, this has also been fixed. Experiment 9 required 1 manual intervention to clear the traversability map due to a false-positive obstacle blocking the way. In experiment 10, the robot is navigating to the goal without correction from the path tracking loop. In this open-loop mode, the robot quickly deviates into obstacles, requiring two manual interventions until ultimately colliding with an obstacle. This comparison shows the utility of exteroception to reduce path tracking errors but also highlights the system’s ability to make progress purely on proprioception.

V. CONCLUSIONS AND LESSONS LEARNED

A. Lessons Learned

- As discussed in eq. 5, the controllability of the motion controller depends on the contact state and robot shape. Experiments at Big Bear showed significant degradation in tracking performance of the motion controller when the robot was close to pencil configuration with non-uniform distribution of screw contacts. Implementing an active compliance controller to ensure a more uniform distribution of normal reaction force or avoiding shapes close to a pencil could mitigate this issue.
- Another compelling alternative solution could be to optimize the screw geometric parameters, which can be a pretty high-dimensional problem. A couple of specific trends are evident from the qualitative analysis of the above experiments: i) increase in screw pitch

Test No.	Field Location	Terrain Geometry	Material	Gait	Distance Traversed (m)	Time (s)	Avg. Speed (cm/s)
1	Table Mountain	30° slope	Unconsolidated Snow	Leader Follower	5.3	103	5.2
2	Table Mountain	Flat and rough, with bumps	Hard Ice	Leader Follower	5.6	150	3.7
3	Table Mountain	Undulating Terrain	Consolidated Snow	Leader Follower	4.0	53	7.6
4	Mars Yard	20° slope	Unconsolidated Sand	Leader Follower	1.4	64	2.2
5	Mars Yard	Flat terrain with small rocks	Consolidated Sand	Sidewinding	1.0	32	3.1
6	Big Bear	Trench	Unconsolidated Snow	Sidewinding	2.5	249	1.0

TABLE I: Field demonstrations of proprioceptive gaits.

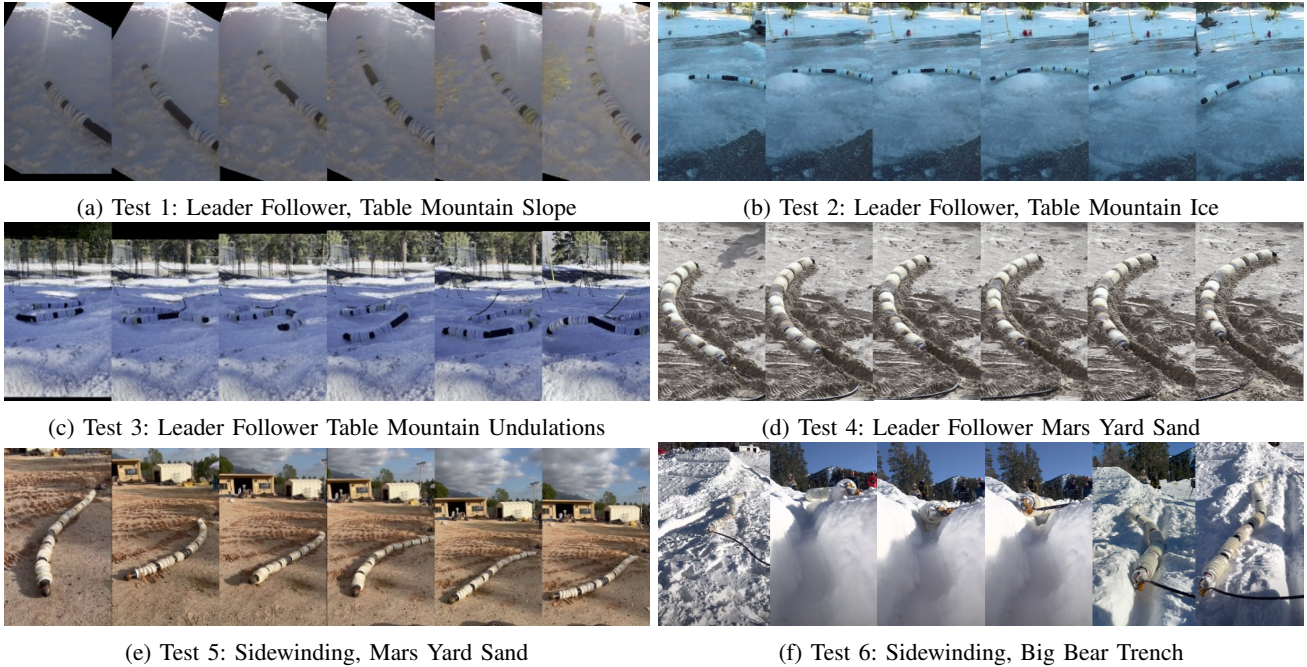


Fig. 7: Timelapse imagery of the field experiments of the proprioceptive gaits

No.	Ext. + Prop.	Obs.	Dist. (m)	Re-plans	Inter-ventions	Error (m)		
						Mean	Std.	Max
1	Y	N	5.32	0	0	0.051	0.035	0.140
2	Y	N	5.31	0	0	0.067	0.033	0.144
3	Y	N	5.64	0	0	0.060	0.042	0.186
4	Y	N	5.45	0	0	0.019	0.016	0.160
5	Y	N	5.31	0	0	0.054	0.036	0.148
6	Y	Y	7.14	1	0	0.027	0.031	0.300
7	Y	Y	5.18	5	3	0.024	0.030	0.142
8	Y	Y	7.91	7	0	0.024	0.025	0.290
9	Y	Y	5.58	4	1	0.029	0.030	0.300
10	N	Y	6.70	0	2	N/A	N/A	N/A

TABLE II: Indoor demonstrations of autonomous navigation with obstacles using exteroceptive gaits on synthetic ice.

- presents greater traction on steep slopes, but decreased control authority to move sideways, and ii) increase in screw length presents greater traction, specifically in unconsolidated media.
- Screws don't work for extremely unconsolidated material (Fig. 7 Test 6). This is because the no-slip constraint along the direction perpendicular to the screws doesn't hold. This makes shape-based gaits the ideal choice for such terrains. Also, exploring a screw design that acts more like propellers (e.g. larger radius and thread depth)



Fig. 8: Experimental setup for exteroceptive gaits experiments 6-10. Autonomy algorithm visualization is shown in top left.

could be another interesting alternative.

- Shape-based gaits make it difficult to stabilize and ensure the safety of the sensor head, warranting a need for gaits that simultaneously stabilize the head while complying with the structure of the terrain.

B. Conclusions

This paper presented a large-scale multi-model snake-robot mobility system for extreme icy terrain and its NEO

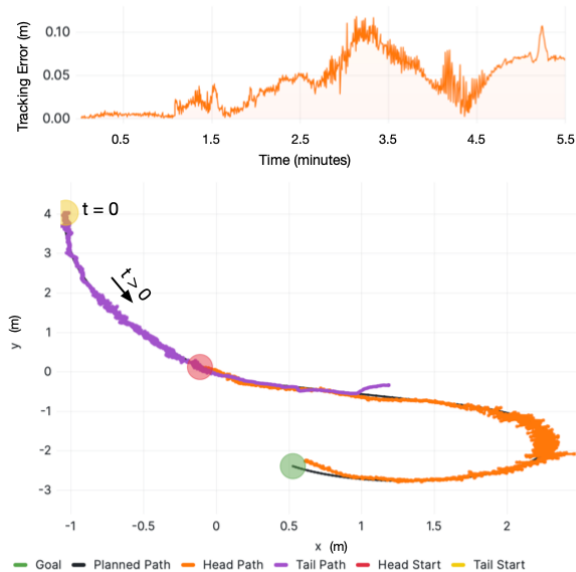


Fig. 9: Planned vs. traversed path (bottom) and tracking error over time (top) for experiment 1

autonomy architecture. We demonstrated the system’s ability to traverse icy, snowy, and sandy environments using both shape- and screw-driven mobility modes with proprioception only. Quantitative experiments showed that exteroceptive closed-loop tracking with screws-based gaits can be achieved with $< 5\text{cm}$ error. This work is a small step towards the development of a platform that is capable of reliable autonomous navigation in extreme ice-world environments to enable the next era of space exploration to discover the origin of life.

VI. ACKNOWLEDGEMENTS

The research was carried out at the Jet Propulsion Laboratory, California Institute of Technology, under a contract with the National Aeronautics and Space Administration (80NM0018D0004).

REFERENCES

- [1] M. Ono, R. Thakker, M. Ingham, K. Carpenter, J. Bowkett, M. Chodas, J. Delaune, R. Etheredge, A. Jasour, J. Jasper, *et al.*, “Autonomy for enceladus vent exploration,” in *2022 Astrobiology Science Conference*. AGU, 2022.
- [2] F. Richter, P. V. Gavrilo, H. M. Lam, A. Degani, and M. C. Yip, “Arcsnake: Reconfigurable snakelike robot with archimedean screw propulsion for multidomain mobility,” *IEEE Transactions on Robotics*, vol. 38, no. 2, pp. 797–809, 2021.
- [3] H. Fukushima, S. Satomura, T. Kawai, M. Tanaka, T. Kamegawa, and F. Matsuno, “Modeling and control of a snake-like robot using the screw-drive mechanism,” *IEEE Transactions on Robotics*, vol. 28, no. 3, pp. 541–554, 2012.
- [4] P. Liljebäck, K. Y. Pettersen, Ø. Stavdahl, and J. T. Gravdahl, “A review on modelling, implementation, and control of snake robots,” *Robotics and Autonomous systems*, 2012.
- [5] J. Liu, Y. Tong, and J. Liu, “Review of snake robots in constrained environments,” *Robotics and Autonomous Systems*, 2021.
- [6] H. Marvi, C. Gong, N. Gravish, H. Astley, M. Travers, R. L. Hatton, J. R. Mendelson III, H. Choset, D. L. Hu, and D. I. Goldman, “Sidewinding with minimal slip: Snake and robot ascent of sandy slopes,” *Science*, vol. 346, no. 6206, pp. 224–229, 2014.

- [7] J. H. LUGO, M. ZOPPI, and R. MOLFINO, “Design and kinematic modeling of a screw-propelled mobile robot to perform remote explosive scent tracing filter sampling in forest during humanitarian demining,” in *Advances in Cooperative Robotics*. World Scientific, 2017, pp. 699–715.
- [8] K. Matsuhiro, K. Tanaka, S. Inoue, T. Zhong, K. Kida, Y. Sugahara, A. Takanishi, and H. Ishii, “Development of small robot with inline archimedean screw mechanism that can move through wetlands,” in *ROMANSY 23-Robot Design, Dynamics and Control: Proceedings of the 23rd CISM IFTOMM Symposium 23*. Springer, 2021, pp. 338–346.
- [9] M. Shikanai, N. Murai, K. Itoh, H. Ishii, A. Akanishi, K. Anoue, S. Ieiri, K. Konishi, and M. Hasizume, “Development of a robotic endoscope that locomotes in the colon with flexible helical fins,” in *2009 Annual International Conference of the IEEE Engineering in Medicine and Biology Society*. IEEE, 2009, pp. 5126–5129.
- [10] T. Dachlika and D. Zarrouk, “Mechanics of locomotion of a double screw crawling robot,” *Mechanism and Machine Theory*, vol. 153, p. 104010, 2020.
- [11] T. Lew, T. Emmei, D. D. Fan, T. Bartlett, A. Santamaria-Navarro, R. Thakker, and A.-a. Agha-mohammadi, “Contact inertial odometry: collisions are your friends,” in *Robotics Research: The 19th International Symposium ISRR*. Springer, 2022, pp. 938–958.
- [12] A. Santamaria-Navarro, R. Thakker, D. D. Fan, B. Morrell, and A.-a. Agha-mohammadi, “Towards resilient autonomous navigation of drones,” in *Robotics Research: The 19th International Symposium ISRR*. Springer, 2022, pp. 922–937.
- [13] P. L. García, S. Crispel, E. Saerens, T. Verstraten, and D. Lefeber, “Compact gearboxes for modern robotics: A review,” *Front. in Rob. and AI*, 2020.
- [14] C. Wright, A. Buchan, B. Brown, J. Geist, M. Schwerin, D. Rollinson, M. Tesch, and H. Choset, “Design and architecture of the unified modular snake robot,” in *2012 IEEE international conference on robotics and automation*. IEEE, 2012, pp. 4347–4354.
- [15] M. Tesch, K. Lipkin, I. Brown, R. Hatton, A. Peck, J. Rembisz, and H. Choset, “Parameterized and scripted gaits for modular snake robots,” *Advanced Robotics*, vol. 23, no. 9, pp. 1131–1158, 2009.
- [16] “Elmo motion control,” <https://www.elmocom.com/>, accessed: 2023-02-327.
- [17] “Cia® 402 series: Canopen device profile for drives and motion control,” <https://www.can-cia.org/can-knowledge/canopen/cia402/>, accessed: 2023-02-327.
- [18] A. Brinkman, J. Morris, I. Chen, N. Sheikh, and P. Warren, “Fastcat: An open-source library for composable ethercat control systems,” in *2021 IEEE Aerospace Conference (50100)*, 2021, pp. 1–8.
- [19] L. E. Dubins, “On curves of minimal length with a constraint on average curvature, and with prescribed initial and terminal positions and tangents,” *American Journal of mathematics*, vol. 79, no. 3, pp. 497–516, 1957.
- [20] M. P. Strub and J. D. Gammell, “Advanced BIT* (ABIT*): Sampling-based planning with advanced graph-search techniques,” in *Proceedings of the IEEE International Conference on Robotics and Automation (ICRA)*, 2020, pp. 130–136.
- [21] I. A. Şucan, M. Moll, and L. E. Kavraki, “The Open Motion Planning Library,” *IEEE Robotics Automation Magazine*, vol. 19, no. 4, pp. 72–82, Dec 2012.
- [22] J. H. Halton, “On the efficiency of certain quasi-random sequences of points in evaluating multi-dimensional integrals,” *Numerische Mathematik*, vol. 2, no. 1, pp. 84–90, Dec 1960.
- [23] J. D. Gammell, T. D. Barfoot, and S. S. Srinivasa, “Informed sampling for asymptotically optimal path planning,” *IEEE Transactions on Robotics (T-RO)*, vol. 34, no. 4, pp. 966–984, 2018.
- [24] B. K. Horn, H. M. Hilden, and S. Negahdaripour, “Closed-form solution of absolute orientation using orthonormal matrices,” *JOSA A*, vol. 5, no. 7, pp. 1127–1135, 1988.
- [25] W. Talbot, J. Nash, M. Paton, E. Ambrose, B. Metz, R. Thakker, R. Etheredge, M. Robinson, M. Ono, and V. Ila, “Analysis of icp covariance estimation methods in perceptually degraded environments for the eels mission concept,” in *IROS*, 2023.
- [26] R. Thakker, N. Alatur, D. D. Fan, J. Tordesillas, M. Paton, K. Otsu, O. Toupet, and A.-a. Agha-mohammadi, “Autonomous off-road navigation over extreme terrains with perceptually-challenging conditions,” in *Experimental Robotics: The 17th International Symposium*. Springer, 2021, pp. 161–173.
- [27] P. Fankhauser, M. Bloesch, and M. Hutter, “Probabilistic terrain

mapping for mobile robots with uncertain localization," *IEEE Robotics and Automation Letters (RA-L)*, vol. 3, no. 4, pp. 3019–3026, 2018.